Does the Fundamental Metallicity Relation Evolve with Redshift? A Perspective From Cosmological Simulations

Alex M. Garcia[1]⋆, Paul Torrey[1], Sara Ellison[2], Kathryn Grasha[4,5,6]†, Lars Hernquist[3], Henry R.M. Zovaro[4,5], Qian-Hui Chen[4,5], Z.S. Hemler[7], Lisa J. Kewley[3], Erica J. Nelson[8], Ruby J. Wright[9]

[1]*Department of Astronomy, University of Virginia, Charlottesville, VA 22904, USA*
[2]*Department of Physics & Astronomy, University of Victoria, Finnerty Road, Victoria, British Columbia, V8P 1A1, Canada*
[3]*Institute for Theory and Computation, Harvard-Smithsonian Center for Astrophysics, Cambridge, MA 02138, USA*
[4]*Research School of Astronomy & Astrophysics, Australian National University, Canberra, Australia, 2611*
[5]*ARC Centre of Excellence for All Sky Astrophysics in 3 Dimensions (ASTRO 3D), Australia*
[6]*Visiting Fellow, Harvard-Smithsonian Center for Astrophysics, 60 Garden Street, Cambridge, MA 02138, USA*
[7]*Department of Astrophysical Sciences, Princeton University, Peyton Hall, Princeton, NJ, 08544, USA*
[8]*Department for Astrophysical and Planetary Science, University of Colorado, Boulder, CO 80309, USA*
[9]*Department of Physics, University of Helsinki, Gustaf Hällströmin katu 2, FI-00014 Helsinki, Finland*

ABSTRACT

The scatter about the mass metallicity relation (MZR) has a correlation with the star formation rate (SFR) of galaxies. The lack of evidence of evolution in correlated scatter at $z \lesssim 2.5$ leads many to refer to the relationship between mass, metallicity, and SFR as the Fundamental Metallicity Relation (FMR). Yet, recent high-redshift ($z > 3$) *JWST* observations have challenged the fundamental (i.e., redshift-invariant) nature of the FMR. In this work, we show that the cosmological simulations Illustris, IllustrisTNG, and EAGLE all predict MZRs that exhibit scatter with a secondary dependence on SFR up to $z = 8$. We introduce the concept of a "strong" FMR, where the strength of correlated scatter does not evolve with time, and a "weak" FMR, where there *is* some time evolution. We find that each simulation analysed has a weak FMR – there is non-negligible evolution in the strength of the correlation with SFR. Furthermore, we show that the scatter is reduced an additional ∼10-40% at $z \gtrsim 3$ when using a weak FMR, compared to assuming a strong FMR. These results highlight the importance of avoiding coarse redshift binning when assessing the FMR.

Key words: galaxies: high-redshift – galaxies: abundances – galaxies: evolution

1 INTRODUCTION

The metal content of galaxies provides key insights into galaxy evolution. Stellar winds and supernovae explosions eject metals formed in stars into the interstellar medium (ISM). Metals then mix via galactic winds (e.g., Lacey & Fall 1985; Koeppen 1994) and turbulence (e.g., Elmegreen 1999) within the disc while pristine gas accretion from the circumgalactic medium (CGM) and outflows dilute the metal content (e.g., Somerville & Davé 2015). Thus, the metal content (metallicity) of the gas within a galaxy is sensitive to such processes, providing a window into the evolutionary processes within a galaxy (Dalcanton 2007; Kewley et al. 2019; Maiolino & Mannucci 2019).

Evidence for the sensitivity of metal content to the gas dynamics within a galaxy is perhaps most clearly seen within the relationship between the stellar mass of a galaxy and its gas-phase metallicity. This mass-metallicity relationship (MZR) describes a relationship of increasing metal content in galaxies with increasing stellar mass (Tremonti et al. 2004; Lee et al. 2006). At low stellar masses, the MZR

relationship is well-described as a power-law, whereas at high masses ($\log[M_*/M_\odot] > 10.5$) the MZR plateaus (e.g., Tremonti et al. 2004; Zahid et al. 2014; Blanc et al. 2019). Furthermore, at a fixed stellar mass, low (high) metallicity galaxies have systematically elevated (depressed) gas masses (Bothwell et al. 2013; Scholte & Saintonge 2023) and SFRs (Ellison et al. 2008; Mannucci et al. 2010). The inverse relationship between a galaxy's metal content and SFR (or gas content) at a fixed stellar mass has been seen in the gas-phase in observations (e.g., Lara-López et al. 2010; Bothwell et al. 2016; Yang et al. 2024) and simulations (e.g., De Rossi et al. 2017; Torrey et al. 2018) as well as for stellar metallicities in simulations (De Rossi et al. 2018; Fontanot et al. 2021; Garcia et al. 2024; Looser et al. 2024) and recent observations (Looser et al. 2024). This secondary dependence on SFR and gas content is qualitatively well-described with basic competing physical drivers: (i) as new pristine gas is accreted onto a galaxy, it drives galaxies toward higher gas fractions, higher star formation rates (SFRs), and lower metallicities, while (ii) galaxies will persistently tend to consume gas and produce new metals, driving galaxies toward lower gas fractions, lower SFRs, and higher metallicities (e.g., Davé et al. 2011; Dayal et al. 2013; Lilly et al. 2013; De Rossi et al. 2015; Torrey et al. 2018). It is

⋆ E-mail: alexgarcia@virginia.edu
† ARC DECRA Fellow

therefore expected that secondary dependence would remain present for galaxies across a wide redshift range given the ubiquity of these physical drivers.

At higher redshift the MZR has been seen to persist (albeit with a lowered overall normalisation e.g., Savaglio et al. 2005; Maiolino et al. 2008; Zahid et al. 2011; Langeroodi et al. 2023) along with the secondary dependence on SFR (e.g., Belli et al. 2013; Salim et al. 2015; Sanders et al. 2018, 2021). Critically, it has been put forth that a single, redshift-invariant plane can be used to describe both the general evolution of the MZR as well as the secondary correlations (Mannucci et al. 2010). This single surface/relation that can describe the metallicity of galaxies over a wide mass and redshift range is referred to as the fundamental metallicity relation (FMR). Recently, however, *JWST* observations have challenged the claim that the FMR can describe galaxies at $z > 3$ (Heintz et al. 2023; Curti et al. 2023; Langeroodi & Hjorth 2023; Nakajima et al. 2023).

To remain truly redshift invariant, the FMR must capture two distinct features of the MZR simultaneously: (i) the existence of a secondary relationship with SFR at fixed redshift, and (ii) the redshift evolution (or lack thereof) in the normalisation. It is therefore possible that a change in either the MZR's secondary correlation with SFR or the redshift evolution of the normalisation of the MZR (or perhaps a combination thereof) may indicate FMR evolution. Many of the previously mentioned studies investigating high-redshift galaxy populations apply a $z \sim 0$ calibrated FMR to higher redshift data (e.g., Mannucci et al. 2010; Wuyts et al. 2012; Belli et al. 2013; Sanders et al. 2021; Curti et al. 2023; Langeroodi & Hjorth 2023; Nakajima et al. 2023). However, it is unclear how to effectively decouple (and subsequently interpret) the observed evolution at high redshift in these frameworks. Some work has been done up to this point observationally looking at higher redshifts independently to specifically isolate the scatter about the MZR (e.g., Salim et al. 2015; Sanders et al. 2015, 2018; Pistis et al. 2023). These works find that there may be some evolution within the scatter about the MZR at intermediate redshifts (Pistis et al. 2023 suggest potentially as low at $z \sim 0.63$). Yet, there are comparatively few simulations results on a systematic examinations on the strength of the secondary dependence on gas content and/or SFR at individual redshifts.

In this work, we investigate the redshift evolution of the MZR's secondary dependence on SFR from the perspective of the cosmological simulations Illustris, IllustrisTNG, and EAGLE. The rest of the paper is as follows: In §2 we describe the simulations we use, our galaxy selection criteria, and summarize definitions of the FMR. In §3 we present the redshift evolution of the FMR as found in simulations. In §4 we quantify the impact of the new framework on the scatter about the MZR, discuss the advantages and challenges in the new framework, and then discuss potential impacts of the physical models. Finally, in §5 we present our conclusions.

2 METHODS

We use the Illustris, IllustrisTNG, and EAGLE cosmological simulations to investigate the dependence of the gas-phase metallicity on stellar mass and star formation. Each of these simulations has a sub-grid ISM pressurisation model, which creates "smooth" stellar feedback. We believe that generic results from all three of these simulations should constitute a fair sampling of predictions from subgrid ISM pressurisation models owing to the appreciably different physical implementations.

Here we briefly describe each of the simulations from this analysis, the galaxy selection criteria we employ, and present a new framework

for interpreting the Mannucci et al. (2010; hereafter M10) FMR projection. All measurements are reported in physical units.

2.1 Illustris

The original Illustris suite of cosmological simulations (Vogelsberger et al. 2013, 2014a,b; Genel et al. 2014; Torrey et al. 2014) was run with the moving-mesh code AREPO (Springel 2010). The Illustris model accounts for many important astrophysical processes, including gravity, hydrodynamics, star formation/stellar evolution, chemical enrichment, radiative cooling and heating of the ISM, stellar feedback, black hole growth, and AGN feedback. The unresolved star forming ISM uses the Springel & Hernquist (2003) equation of state, wherein new star particles are created from regions of dense ($n_H > 0.13 \, \mathrm{cm}^{-3}$) gas. The masses of the stars within the star particle are drawn from a Chabrier (2003) initial mass function (IMF) and metallicities are adopted from the ISM where they are born. As the stars evolve, they eventually return their mass and metals back into the ISM. The stellar mass return and yields used allow for the direct simulation of time-dependent return and heavy metal enrichment, explicitly tracking nine different chemical species (H, He, C, N, O, Ne, Mg, Si, and Fe).

The Illustris suite consists of a single volume of size $(106.5 \, \mathrm{Mpc})^3$ at three different resolutions. The three resolutions are as follows: Illustris-1 (2×1820^3 particles), Illustris-2 (2×910^3 particles), and Illustris-3 (2×455^3 particles). We use Illustris-1, the highest resolution run, which is hereafter we refer to synonymously with Illustris itself.

2.2 IllustrisTNG

IllustrisTNG (The Next Generation; Marinacci et al. 2018; Naiman et al. 2018; Nelson et al. 2018; Pillepich et al. 2018b; Springel et al. 2018; Pillepich et al. 2019; Nelson et al. 2019a,b, hereafter TNG) is the successor to the original Illustris simulations, alleviating some of the deficiencies of and updating the original Illustris model. As such, the Illustris and TNG models are similar, yet have an appreciably different physical implementation (see Weinberger et al. 2017; Pillepich et al. 2018a, for a complete list of differences between the models). A critical difference between the Illustris and TNG models for the context of this work is TNG's implementation of redshift-scaling winds. The TNG model employs a wind velocity floor not present in the original Illustris model in order to prevent low mass haloes from having unphysically large mass loading factors. Consequently, low redshift star formation is suppressed in the TNG model. TNG implements the same equation of state for the dense star forming ISM as Illustris (Springel & Hernquist 2003). As in Illustris, new star particles are created from dense gas using the Chabrier (2003) IMF. Furthermore, TNG tracks the same nine chemical species as Illustris, while also following a tenth "other metals" as a proxy for metals not explicitly monitored.

TNG consists of three different volumes each with their own subresolution runs: TNG50 $(51.7 \, \mathrm{Mpc})^3$, TNG100 $(110.7 \, \mathrm{Mpc})^3$, and TNG300 $(302.6 \, \mathrm{Mpc})^3$. In this work, we will use the highest resolution TNG100 run (TNG100-1; hereafter used synonymously with TNG), with 2×1820^3 particles, as a comparable volume and resolution to the original Illustris.

2.3 EAGLE

Unlike Illustris and TNG, "Evolution and Assembly of GaLaxies and their Environment" (EAGLE, Crain et al. 2015; Schaye et al. 2015; McAlpine et al. 2016) employs a heavily modified version of the smoothed particle hydrodynamics (SPH) code GADGET-3 (Springel 2005; ANARCHY, see Schaye et al. 2015 Appendix A). EAGLE includes many of the same baryonic processes (star-formation, chemical enrichment, radiative cooling and heating, etc) as Illustris and TNG. The dense (unresolved) ISM in EAGLE is also treated with a sub-grid equation of state (Schaye & Dalla Vecchia 2008; hereafter, SDV08), much like that of SH03. The SDV08 prescription forms stars according to a Chabrier (2003) IMF from the dense ISM gas. The density threshold for star formation is given by the metallicity-dependent transition from atomic to molecular gas computed by Schaye (2004). Stellar populations evolve according to the Wiersma et al. (2009) evolutionary model and eventually return their mass and metals back into the ISM. EAGLE explicitly tracks eleven different chemical species (H, He, C, N, O, Ne, Mg, Si, S, Ca, and Fe).

The full EAGLE suite is comprised of several simulations ranging from size $(12 \text{ Mpc})^3$ to $(100 \text{ Mpc})^3$. We use data products at an intermediate resolution $(2 \times 1504^3$ particles) run with a box-size of $(100 \text{ Mpc})^3$ referred to as RefL0100N1504 (hereafter simply EAGLE) as a fair comparison to the selected Illustris and TNG runs.

2.4 Galaxy selection

All three simulations in this work select gravitationally-bound substructures using SUBFIND (Springel et al. 2001; Dolag et al. 2009), which identifies self-bound collections of particles from within friends-of-friends groups (Davis et al. 1985). We limit our analysis to central galaxies that we consider 'well-resolved' (i.e., containing $\sim$100 star particles and $\sim$500 gas particles), thus we restrict the sample to galaxies with stellar mass $\log(M_* \ [M_\odot]) > 8.0$ and gas mass $\log(M_{gas} \ [M_\odot]) > 8.5$. We place an upper stellar mass limit of $\log(M_* \ [M_\odot]) > 12.0$[1]. Following from a number of previous works (see, e.g., Donnari et al. 2019; Nelson et al. 2021; Hemler et al. 2021; Garcia et al. 2023), we exclude quiescent galaxies by defining a specific star formation main sequence (sSFMS). We do so by fitting a linear-least squares regression to the median sSFR-M_* relation with stellar mass $\log(M_* \ [M_\odot]) < 10.2$ in mass bins of 0.2 dex. The sSFMS above $10.2 \log M_\odot$ is extrapolated from the regression. Galaxies that fall greater than 0.5 dex below the sSFMS are not included in our sample. As we show in Garcia et al. (2024; that paper's Appendix B), our key results (using stellar metallicities) are *not* sensitive to our sample selection. We obtain the same result here in the gas-phase: our key results are qualitatively unchanged by the same variations as Garcia et al. (2024) in selection criteria (see Appendix A).

2.5 Definitions of the FMR

M10 propose that the 3D relationship between stellar mass, gas-phase metallicity, and star formation rate (SFR) can be projected into 2D using a linear combination of the stellar mass and star formation:

$$\mu_\alpha = \log M_* - \alpha \log \text{SFR} , \qquad (1)$$

---

[1] The upper mass limit does not exclude any galaxies for most redshifts

$$\mu_\alpha = \log M_* - \alpha \log \text{SFR}$$

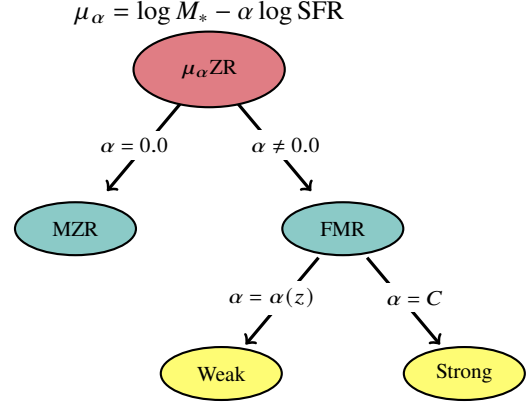**Figure 1. Decision tree for the μ_αZR, see Section 2.5 for full details.** This shows the different relationships that can be included under the umbrella μ_α metallicity relation (μ_αZR; see Equation 1). First is the traditional MZR where $\alpha = 0.0$ and second is the FMR where $\alpha \neq 0.0$. The FMR can be further broken into two categories: strong and weak depending on if α varies as a function of redshift (weak) or not (strong).

where α is a free parameter that ranges from 0 to 1[2]. The free parameter α holds all the diagnostic power on the strength of the MZR's secondary dependence with SFR. By varying α, the distribution of galaxies in μ_α-metallicity space varies. We define a μ_α-metallicity relation (μ_αZR) for each α as a linear-least squares regression[3] of the data. We compute the μ_αZR for $\alpha = 0.0$ to 1.0 in steps of 0.01 and obtain the residuals about each regression. The projection that yields the minimum scatter in the residuals (smallest standard deviation) is deemed the best fit. The α value associated with this minimum scatter projection is henceforth referred to as α_{min}. We define an uncertainty on α_{min} by assuming that a projection that has scatter within 5% of the minimum value is a plausible candidate for the true α_{min} (following from Garcia et al. 2024).

α_{min} physically represents the direction to project the 3D mass-metallicity-SFR ($M_* - Z_{gas} - \text{SFR}$) space into a minimum scatter distribution in 2D $\mu_\alpha - Z$ space. Thus, the μ_αZR is the relation of merit in the 2D projection of the $M_* - Z_{gas} - \text{SFR}$ relation. There are two outcomes, either (i) $\alpha_{min} = 0.0$, wherein the canonical MZR is recovered, or (ii) $\alpha_{min} \neq 0.0$, wherein an FMR is recovered. In this way, the μ_αZR can be thought of as a superset of relations containing the MZR, the strong FMR, and the weak FMR (relationships illustrated in Figure 1). Framing the FMR in this way underscores the decisions required in establishing the FMR. Previous studies have been somewhat restrictive in regards to these decisions. We therefore highlight the need to take a deliberate approach to our definitions to build a framework by which potential redshift evolution can be assessed.

Traditionally (as in, e.g., M10), the FMR is defined by determining α_{min} at $z = 0$. This value has been seen to be roughly constant at

---

[2] Parameterisations exist with more complexity; for example, Curti et al. (2020) introduce a functional form for the FMR (opposed to a 2D projection). We opt to not present other forms of the FMR in this work as a exercise on the extent to which the M10 projection can describe the of scatter at fixed redshift.

[3] M10 use a fourth-order polynomial for fitting. This practice is inconsistent in the literature with many (e.g., Andrews & Martini 2013) considering a linear regression. We show that using a fourth-order polynomial instead of a linear regression does not significantly alter our α_{min} determination in Appendix B.

	Illustris	**TNG**	**EAGLE**
$z = 0$	$0.23^{0.34}_{0.08}$	$0.31^{0.59}_{0.00}$	$0.74^{0.86}_{0.57}$
$z = 1$	$0.33^{0.46}_{0.11}$	$0.61^{0.69}_{0.47}$	$0.73^{0.81}_{0.63}$
$z = 2$	$0.39^{0.52}_{0.20}$	$0.60^{0.67}_{0.47}$	$0.65^{0.75}_{0.52}$
$z = 3$	$0.45^{0.56}_{0.30}$	$0.65^{0.72}_{0.55}$	$0.59^{0.68}_{0.44}$
$z = 4$	$0.49^{0.59}_{0.36}$	$0.68^{0.75}_{0.57}$	$0.53^{0.62}_{0.39}$
$z = 5$	$0.52^{0.61}_{0.39}$	$0.70^{0.77}_{0.59}$	$0.46^{0.56}_{0.33}$
$z = 6$	$0.53^{0.63}_{0.39}$	$0.70^{0.77}_{0.59}$	$0.44^{0.54}_{0.31}$
$z = 7$	$0.56^{0.65}_{0.42}$	$0.70^{0.78}_{0.58}$	$0.40^{0.49}_{0.27}$
$z = 8$	$0.59^{0.69}_{0.47}$	$0.70^{0.78}_{0.58}$	$0.31^{0.42}_{0.16}$

Table 1. All $\alpha_{\min}$ **values at** $z = 0 - 8$ **for Illustris, TNG, and EAGLE.** These $\alpha_{\min}$ values are determined at each redshift individually. The superscripts are the upper limits of the uncertainty while the subscripts are the lower limits. We show these values in Figure 2.

$z \lesssim 2.5$ (e.g., M10; Andrews & Martini 2013). We henceforth refer to the idea that $\alpha_{\min}$ does not vary as a function of redshift as the strong FMR. A single $\alpha_{\min}$ can describe both the MZR's secondary dependence and its normalisation evolution in the strong FMR. In this work, we investigate the claim that $\alpha_{\min}$ is constant over time by identifying the $\alpha_{\min}$ value that minimizes scatter at each redshift independently. This procedure allows $\alpha_{\min}$ to (potentially) vary as a function of redshift. Here we introduce the concept of a "weak" FMR. We define the weak FMR as a counterpoint to the strong FMR: that $\alpha_{\min} \neq 0$, but $\alpha_{\min}$ is *not* constant as a function of redshift (see illustrated relationship in Figure 1).

There are actually more parameters beyond $\alpha_{\min}$ that the FMR is defined by: the parameters of the regression (in our case slope and intercept). These additional parameters add complexity to the interpretation of the evolution. Regressions are inherently linked to the $\alpha_{\min}$ determination, yet the parameters of the fit can have a profound impact on interpretation of FMR evolution irrespective of $\alpha_{\min}$ variations. The impact of these parameters is beyond the scope of this work since we only examine each redshift bin independently here and the effect of the regression parameters is only felt when comparing different redshift bins. We do, however, address the impact of these parameters in a companion work (Garcia et al. in prep).

3 RESULTS

3.1 Does $\alpha_{\min}$ vary as a function of redshift?

We use the best-fit $\alpha_{\min}$ values derived as a function of redshift to evaluate whether the scatter about the MZR evolves significantly with redshift. We find that $\alpha_{\min} \neq 0$ at all redshifts in each of the three simulations (Figure 2). Based on the first step of the decision tree in Figure 1, the non-zero $\alpha_{\min}$ values show there is an FMR in each simulation. The secondary dependence on SFR is present, at least to some extent, within the scatter of all the MZRs analysed here. It should be noted, however, that the uncertainty[4] on the TNG $z = 0$ $\alpha_{\min}$ value does include $\alpha = 0$. This implies a somewhat weak dependence on SFR at this redshift. In Garcia et al. (2024), we attribute a lack of a relationship at $z = 0$ in TNG to the redshift scaling

of winds within the TNG model[5]. Briefly, the effect of adding winds that change with redshift suppresses low redshift star formation and increases the efficiency of high redshift stellar feedback compared to the Illustris model (see Pillepich et al. 2018a). It is therefore likely that the suppressed low redshift star formation causes the large uncertainty on $\alpha_{\min}$ at $z = 0$. As such, features of $\alpha_{\min}$ are sensitive to details of the wind implementation/strength prescribed by the model on which it is built (see Section 4.3 for further discussion).

Overplotted on Figure 2 (gray squares) are three observationally determined values of $\alpha_{\min}$ from M10 (0.32), Andrews & Martini (2013; 0.66), and Curti et al. (2020; 0.55). Each of these values was determined using SDSS galaxies at $z \approx 0$ (offset horizontally for clarity). Deviations in the observational values are attributed primarily to: (i) different metallicity calibrations, (ii) using individual galaxies versus galaxy stacks (as in Andrews & Martini 2013), and (iii) selection biases towards higher star forming galaxies. Simulations are not directly affected by metallicity calibrations in the same way as observations. The sample selection criteria (outlined in Section 2.4) should help mitigate the effect of selection function biases of observations. Though we select star-forming galaxies, we do not just select the highest star forming galaxies. In spite of these potential differences, it is worth noting that the M10 $\alpha_{\min}$ value agrees fairly well with the TNG and Illustris derived values at $z = 0$. Although the uncertainty on the TNG $\alpha_{\min}$ is significant enough to include the Curti et al. (2020) value by a factor of ~ 1.5 times higher. Similarly, the Andrews & Martini (2013) value of 0.66 agrees fairly well with the derived value from EAGLE at $z = 0$, though we caution that this analysis was done with galaxy stacks whereas we us individual galaxies here.

Furthermore, we find that $\alpha_{\min}$ values show some level of redshift evolution in all three simulations (Figure 2 and Table 1). Therefore, from the decision tree of Figure 1, the strong FMR is ruled out in favour of a weak FMR. Interestingly, each simulation has qualitatively different redshift evolution. TNG $\alpha_{\min}$ values vary significantly from $z = 0$ to $z = 1$ but then level off, the Illustris $\alpha_{\min}$ values increase monotonically with redshift, and the EAGLE values decrease monotonically as a function of redshift. Redshift evolution of the derived $\alpha_{\min}$ values may be indicative of evolution in the driving forces of the scatter about MZR.

Our result in EAGLE indicating significant redshift evolution seemingly contradicts a previous study finding the FMR is in place and does not evolve out to $z \approx 5$ in EAGLE (De Rossi et al. 2017). There is a subtle difference in the analysis between the two works, however: De Rossi et al. (2017) do not parameterise the FMR to test $\alpha_{\min}$ variations. They qualitatively examine the secondary dependence within the MZR and show that a $M_*-Z_{gas}-SFR$ relation exists at $z = 0 - 5$ (i.e., there is at least a weak FMR over these redshift ranges). We find that an $M_*-Z_{gas}-SFR$ relation at $z = 0 - 5$ exists in EAGLE via non-zero $\alpha_{\min}$ values (i.e., there is at least a weak FMR over these redshift ranges), consistent with De Rossi et al. (2017). Despite the persistence of the $M_*-Z_{gas}-SFR$ relation, we confirm that there is a weak in EAGLE by using the M10 projection of the FMR. It should be noted that the uncertainty of the $z = 0$ and $z = 5$ values do overlap in EAGLE. The subtly of the redshift evolution may therefore be difficult to detect without fitting each redshift independently.

---

[4] Uncertainties on $\alpha_{\min}$ correspond to the uncertainty in the minimum dispersion (see Section 2.5 for definition)

[5] We show this in Garcia et al. (2024) for *stellar* metallicities. That work also demonstrates that stellar and gas-phase metallicities are related to each other (see Section 4.1 of that work). Therefore, the same physical mechanism suppressing the correlated scatter for stellar metallicities is likely what is suppressing $\alpha_{\min}$ for the gas-phase.
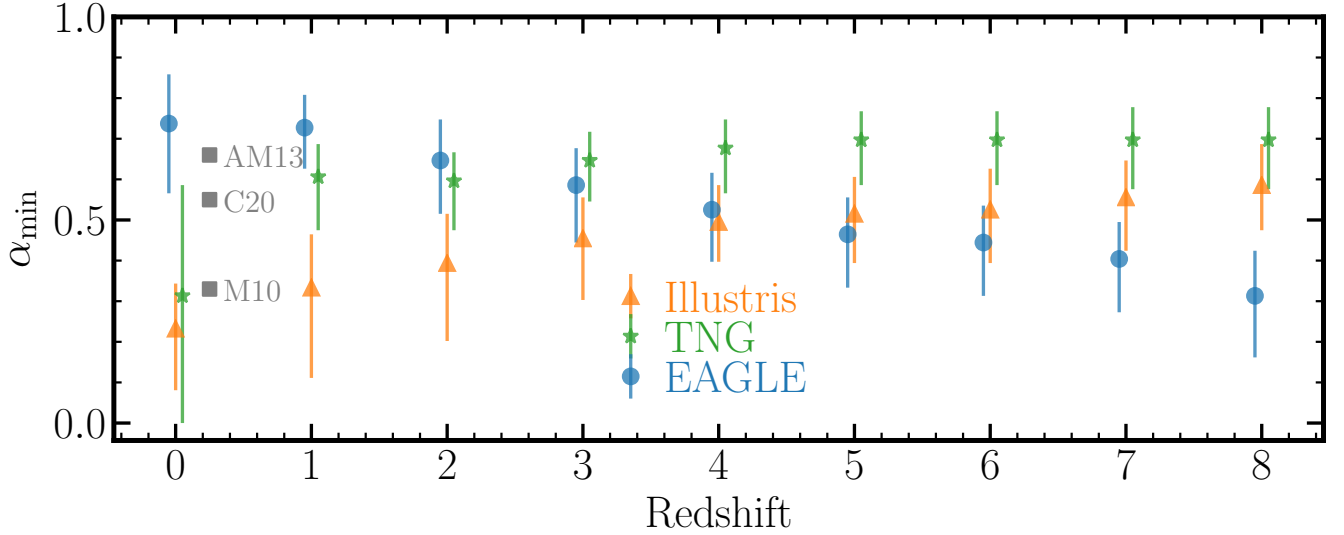
Figure 2. $\alpha_{\min}$ **values as a function of redshift in Illustris, TNG, and EAGLE.** $\alpha_{\min}$ values as a function of redshift are plotted as orange triangles, green stars, and blue circles for Illustris, TNG, and EAGLE, respectively. The errorbars here are obtained by finding α values that reduce the scatter to within 5% that of the minimized scatter. The gray squares are observational values of $\alpha_{\min}$ from M10, Andrews & Martini (2013), and Curti et al. (2020) determined at $z \approx 0$ via SDSS (offset from $z = 0$ for aesthetic purposes).

3.2 Scatter assuming different FMRs

The derived $\alpha_{\min}$ values show that Illustris, TNG, and EAGLE all have weak FMRs. We now examine how the impact of marginalising over variations in $\alpha_{\min}$ when assuming a strong FMR. Specifically, we want to quantify how the scatter changes when assuming a strong versus weak FMR. This will provide a quantitative metric for assessing how important considerations for an evolving FMR are. If the scatter were to remain unchanged, or change only marginally, the need for a weak FMR would be minimal.

To this end, we define three different ratios for quantitatively evaluating the importance of using a weak FMR. We consider ratios of the scatters about: (i) the weak FMR compared to the MZR, (ii) the strong FMR compared to the MZR, and (iii) the weak FMR compared to the strong FMR. Figure 3 illustrates these three different ratios evaluated at each redshift for Illustris (orange diamonds), TNG (green stars), and EAGLE (blue circles).

The left panel of Figure 3 shows the standard deviation of the residuals (henceforth, scatter) about each redshift's weak FMR ($\alpha_{\min}$ determined at that redshift) normalised by the scatter about the MZR ($\alpha_{\min} = 0$) as a function of redshift ($\sigma_{\mathrm{weak}}/\sigma_{\mathrm{MZR}}$). We find for all redshifts across the three simulations that the weak FMR reduces the scatter by $\sim 10 - 30\%$ compared to the MZR. The exception is TNG at $z = 0$ having scatter reduction of less than 5% – falling within the nominal uncertainty on $\alpha_{\min}$ and implying there is functionally no difference between the scatter of the MZR and FMR at this redshift. This $z = 0$ TNG exception was discussed previously in the context of the $\alpha_{\min}$ value (see Section 3.1) and the lack of a relation was attributed to the redshift scaling winds in the TNG model (see Pillepich et al. 2018a). The scatter reduction is roughly constant as a function of redshift in both TNG and EAGLE at around $\sim 20\%$ (barring the aforementioned TNG exception). Scatter reduction in Illustris ranges from $\lesssim 10\%$ at $z = 0$ to nearly 30% at $z = 8$.

The middle panel of Figure 3 shows the scatter at each redshift assuming a strong FMR compared to that of the MZR at that redshift ($\sigma_{\mathrm{strong}}/\sigma_{\mathrm{MZR}}$). We define the strong FMR fit analogously to

observations: we apply a $z = 0$ determined $\alpha_{\min}$ value to all redshifts. In TNG, we find a similar trend to that of $\sigma_{\mathrm{weak}}/\sigma_{\mathrm{MZR}}$: a roughly constant scatter reduction as a function of redshift, albeit at a reduced value of $\sim 5 - 10\%$ (see previous discussion about the exception at $z = 0$). The scatter reduction in Illustris is similarly constant around 10%. Evidently, the redshift evolution in Illustris seen previously with $\sigma_{\mathrm{weak}}/\sigma_{\mathrm{MZR}}$ disappears when assuming a strong FMR. $\sigma_{\mathrm{strong}}/\sigma_{\mathrm{MZR}}$ actually *increases* nearly monotonically in EAGLE as a function of redshift: the strong FMR fit on the low redshift bins is significantly better than the highest redshifts. Remarkably, assuming a strong FMR actually begins to increase the scatter by $10 - 40\%$ compared to the MZR at high redshift ($z > 5$) in EAGLE. The concept of an FMR is one that relies on minimizing scatter compared to the MZR, yet at the highest redshifts in EAGLE it achieves the opposite. This is a clear failure of the strong FMR in EAGLE as well as a cautionary tale for interpreting future high-redshift FMR observations.

Finally, the right panel of Figure 3 shows the ratio of the scatter of the weak FMR divided by the scatter of the strong FMR evaluated at each redshift ($\sigma_{\mathrm{weak}}/\sigma_{\mathrm{strong}}$). The ratio $\sigma_{\mathrm{weak}}/\sigma_{\mathrm{strong}}$ is of particular interest as it provides a diagnostic for how well an assumed strong FMR characterises galaxies at higher redshift compared to their minimum scatter projection. The ratio is unity at $z = 0$ by construction, since the strong FMR assumes the $z = 0$ $\alpha_{\min}$ value for all redshifts. In Illustris and EAGLE, the scatter reduction of the weak FMR at $z \leq 2$ is less than 5%. The relatively low decrease in the scatter in these two simulations implies that the strong FMR might approximately hold at these low redshifts (qualitatively consistent with previous observational findings; M10; Cresci et al. 2019). The scatter reduction at $z \geq 3$, however, is $\gtrsim 10\%$ for Illustris and EAGLE. Both have monotonically decreasing ratios of scatter in the high-z regime out to a 20% decrease in Illustris and nearly 40% in EAGLE. On the other hand, the scatter reduction in TNG stays roughly constant at around 15% at $z > 0$.

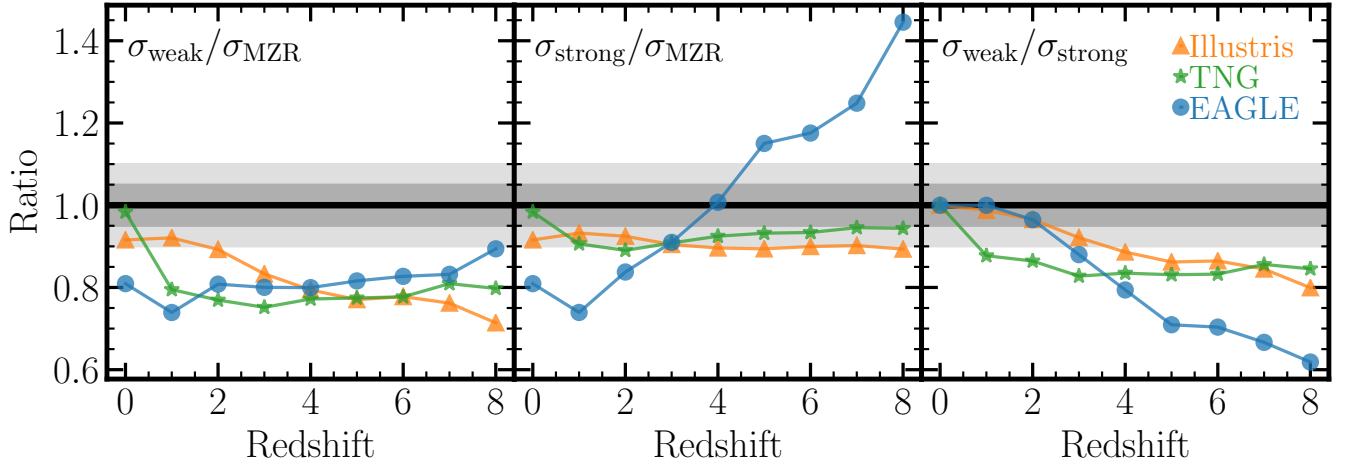Overall, the 10-40% decrease in using a weak FMR indicates that

Figure 3. Reduction in scatter for weak FMR versus MZR, strong FMR versus MZR, and weak FMR versus strong FMR. *Left:* the scatter about the FMR by fitting $\alpha_{\min}$ at each redshift individually (σ_{weak}) divided by the scatter in the MZR at each redshift (σ_{MZR}) as a function of redshift. The dark and light gray shaded regions (in all panels) represent 5% and 10% variations, respectively, of each ratio. *Centre:* Same as left, but now the numerator is the scatter about the FMR evaluated in each redshift bin with a $z = 0$ calibrated $\alpha_{\min}$ (σ_{strong}). *Right:* Previous two panels divided by each other, the reduction in scatter in the relationship by determining $\alpha_{\min}$ at each redshift independently (σ_{weak}) divided by using the $z = 0$ $\alpha_{\min}$ value (σ_{strong}).

high redshift galaxy populations are different from the low redshift systems. The strong FMR does not effectively characterise these high redshift galaxies. This marked shift in efficacy of the strong FMR further supports the idea there is some time evolution within the FMR in Illustris, TNG, and EAGLE.

It is worth noting how deceptive the lack of evolution in the strong FMR scatter reduction ratio (central panel of Figure 3) is for Illustris and TNG. Looking at the reduction in scatter of the strong FMR by itself in these two simulations may lead one to conclude that a strong FMR holds – the strong FMR does reduce scatter at all redshifts, even by a roughly constant amount. Indeed it is remarkable that the strong FMR reduces the scatter by a similar amount at $z = 0$ as $z = 8$ despite ignoring a variation of a factor of > 2 in $\alpha_{\min}$. However, we emphasize that using the weak FMR significantly improves the characterisation of these galaxy populations, particularly at high redshift.

In summary, by determining $\alpha_{\min}$ at each redshift independently, we find that the scatter can be reduced an additional $\sim 10 - 40\%$ compared to an assumed strong FMR. We therefore conclude that the variations in $\alpha_{\min}$ are significant, particularly at high redshift. The significant variations past $z \gtrsim 3$ seem to imply that the strong FMR is not even a good approximation in the early universe in our simulations.

4 DISCUSSION

4.1 What do variations in $\alpha_{\min}$ mean?

The main idea of the FMR comes from the idea that in the MZR, at a fixed stellar mass, the metallicities and SFRs of galaxies are anti-correlated. Using $\alpha_{\min}$ is an attempt to represent the strength of the correlation between metallicity and SFR; however, it does not actually explicitly tell us about that relationship. Rather, $\alpha_{\min}$ values are tuned to minimize scatter. It is therefore critical to develop an understanding of the strength of the correlation between metallicity and star formation rates that is not just a scatter-minimisation tool. To build this understanding, we first take the FMR regression as defined

in Section 2.5:

$$Z = m \left(\log M_* - \alpha_{\min} \log \text{SFR} \right) + b \,, \qquad (2)$$

where m is the slope of the regression and b is the intercept[6]. By defining $\Delta Z = Z - \langle Z_{\text{MZR}} \rangle$ (i.e., a galaxy's offset from the MZR is the metallicity of the galaxy subtracted from the MZR value at that galaxy's stellar mass) and take a thin mass bin, such that $\log M_* \approx C$, we can rearrange Equation 2 to obtain

$$\Delta Z = m(-\alpha_{\min} \log \text{SFR}) + b' \,, \qquad (3)$$

where $b' = b + mC - \langle Z_{\text{MZR}} \rangle$. Equation 3 is a statement that, at fixed stellar mass, metallicity is anti-correlated with $\log$ SFR by a factor of $m\alpha_{\min}$. Here we have an explicit relationship between off-sets from the MZR and the SFR of galaxies. Conveniently, ΔZ is proportional to $-\alpha_{\min}$, our scatter minimisation parameter. A key prediction here is that a strong FMR (no $\alpha_{\min}$ variations) should keep a constant relationship between offsets and SFR across time, whereas the weak FMR predicts a changing relationship[7]. The key advantage of considering FMR variations in ΔZ-log SFR space is in its interpretability. We gain the same qualitative understanding by a smaller/larger $\alpha_{\min}$ value at high redshift, but in this framework it is more straight-forward to see how the relationship between metallicity and SFR changes with time.

To demonstrate ΔZ's scaling with SFR, we take a thin mass bin of width 0.5 dex ($10^{8.0} < M_* \, [M_\odot] < 10^{8.5}$) and measure the offsets from the MZR as a function of SFR for all three simulations (see Figure 4). We note that these are qualitatively similar to the "deviation plots" of ΔZ and Δ specific SFR in Davé et al. (2017). We determine the MZR from the median metallicity in fixed mass bins

---

[6] Note that we assume a linear regression here, but others (e.g., M10) use a fourth-order regression. We show that our choice of first-order does not significantly impact our results in Appendix B

[7] We note, however, that while $\alpha_{\min}$ is *related* to the strength of the (anti-) correlation between ΔZ and SFR, in actuality, there is another scaling with the slope of the FMR (m)
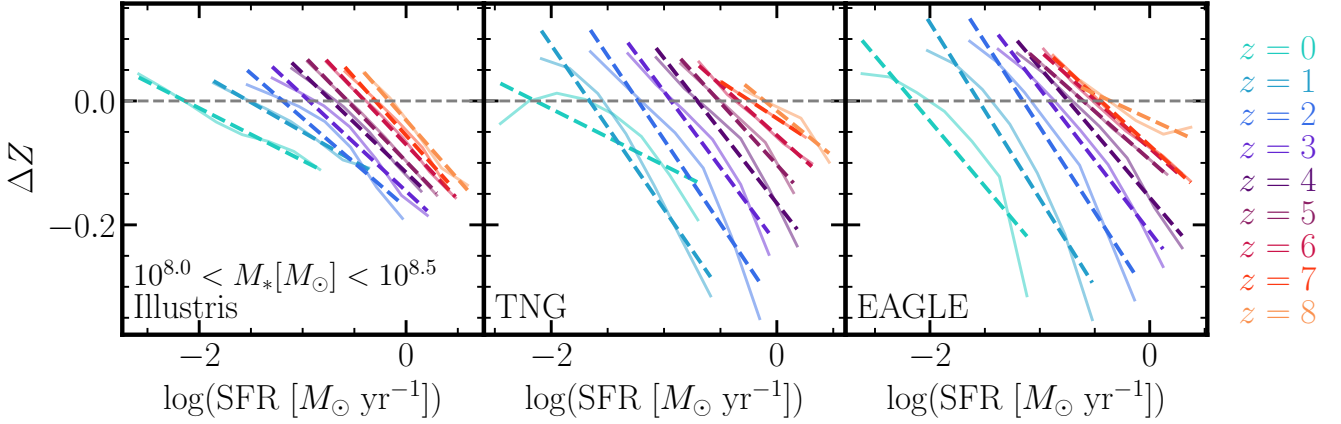
Figure 4. Offsets from the MZR as a function of SFR in a thin mass bin for $z = 0 - 8$ **in Illustris, TNG, and EAGLE.** The redshift evolution of the offsets from the MZR, ΔZ, as a function of SFR for Illustris (left), TNG (centre), and EAGLE (right) for galaxies with stellar mass $10^{8.0} < M_* \, [M_\odot] < 10^{8.5}$. The thin solid lines are the median offsets in fixed SFR bins of width 0.5 dex. The dashed lines are a linear regression of the medians. The different coloured lines are the different redshifts (left-to-right in an individual panel is $z = 0 - 8$).

of width 0.05 dex. The offsets from the MZR, ΔZ, are then generated by interpolating the MZR at each galaxy's stellar mass.

We find that, at all redshifts in each simulation, the offsets from the MZR are anti-correlated with SFR, as expected. Furthermore, we find qualitative agreement between the slope of this anti-correlation and $\alpha_{\min}$ values. In Illustris (left panel of Figure 4), we find that the slope is shallow at $z = 0$ and gets steeper with increasing redshift. This behaviour is consistent with the $\alpha_{\min}$ variations seen in Illustris – $\alpha_{\min}$ is small at $z = 0$ in Illustris and increases with increasing redshift (see Figure 2). We find that the $z = 0$ slope in TNG is significantly weaker than the $z > 0$ slopes (central panel of Figure 4), consistent with the $\alpha_{\min}$ values from TNG. It should be noted, however, that the $\alpha_{\min}$ values at $z \geq 5$ are all the same, whereas the slopes of ΔZ versus SFR change slightly at $z \geq 5$. Finally, in EAGLE, we find that the slope of ΔZ versus SFR is steepest at $z = 0$ and shallows with increasing redshift, again consistent with behaviour in $\alpha_{\min}$ as a function of redshift. We emphasize that there is an additional term, m (the slope of the FMR regression from Equation 2), included in the slope of ΔZ versus SFR. We therefore caution against too strong a comparison against $\alpha_{\min}$ and slopes in ΔZ-SFR space. Changes in the slope of the FMR may cause a change in the slope of ΔZ versus SFR. ΔZ is only *proportional to* $\alpha_{\min} \log$ SFR.

In summary, the slope between offsets from the MZR and SFR offers a more straight-forward way to understand the (potential) evolution in the relationship between metallicity and SFR suggested by $\alpha_{\min}$ variations.

4.2 Advantages and challenges of a weak FMR Framework

The key advantage of fitting each redshift independently is to more effectively minimize the scatter. The weak FMR gives us a clear-cut metric for the strength of the MZR's secondary dependence on SFR arises that is completely independent of the evolution of the normalisation of the MZR. Independence from other redshift populations removes the possibility of conflating evolution of the normalisation of the MZR with evolution of the scatter. By using a $z = 0$ derived $\alpha_{\min}$ at all redshifts (i.e., strong FMR) we suppress any potential variation of $\alpha_{\min}$ as a function of redshift. As a consequence, the strong FMR does not optimally reduce scatter across redshift (dis-

cussed in more detail in Section 3.2). Using a weak FMR assumption therefore allows a more careful examination for the extent to which the observed FMR has variations.

A challenge of performing a similar analysis in observations is the amount of data available. For example, lower redshift galaxy populations are well sampled (e.g., M10 use 141,825 SDSS $z \sim 0$ galaxies), but at higher redshift sampling becomes more difficult (e.g., the Nakajima et al. 2023 and Curti et al. 2023 analyses use less than 200 objects spanning a wider redshift range of $z = 3 - 10$). It is possible that subtle changes can be measured at lower redshifts (see Pistis et al. 2023 for a potential detection of MZR scatter variations at $z \sim 0.63$); however, the most significant scatter reduction happens in the high redshift ($z \gtrsim 3$) populations (Figures 3). More complete samples of galaxy populations at these early times with, e.g., JWST are therefore required in order to undergo any weak FMR-style analysis to detect significant deviations from the $z = 0$ $\alpha_{\min}$ values. Moreover, a redshift-complete sample would be limited by our understanding of metallicity in the high redshift universe. Recently, work has been done to obtain reliable metallicity diagnostics at $z > 4$ using *JWST*/NIRSpec (e.g., Nakajima et al. 2023; Sanders et al. 2023; Shapley et al. 2023). However, more complete galaxy samples are required, particularly at the low metallicities seen at this epoch, to fully characterise these diagnostics. As such, it is currently difficult to ensure that $\alpha_{\min}$ values determined observationally are fair comparisons across the broad redshift range examined in this work.

4.3 Dependence on small scale physics implementations

We find that Illustris, TNG, and EAGLE have weak FMRs. The $\alpha_{\min}$ values are not the same, nor do they evolve in the same fashion, in the different models, however. The value of $\alpha_{\min}$ at any given redshift is a complicated by-product of a number of different physical processes. While we have some qualitative understanding of how $\alpha_{\min}$ is set (or changed), the exact mechanisms $\alpha_{\min}$ are not entirely clear in detail.

What is clear is that $\alpha_{\min}$ is sensitive to the physics driving galaxy evolution. For example, in Section 3.1, we attributed the lowered $\alpha_{\min}$ values in TNG at $z = 0$ to the redshift-dependent wind prescription in the TNG model (as mentioned in Section 3.1). Through this example,
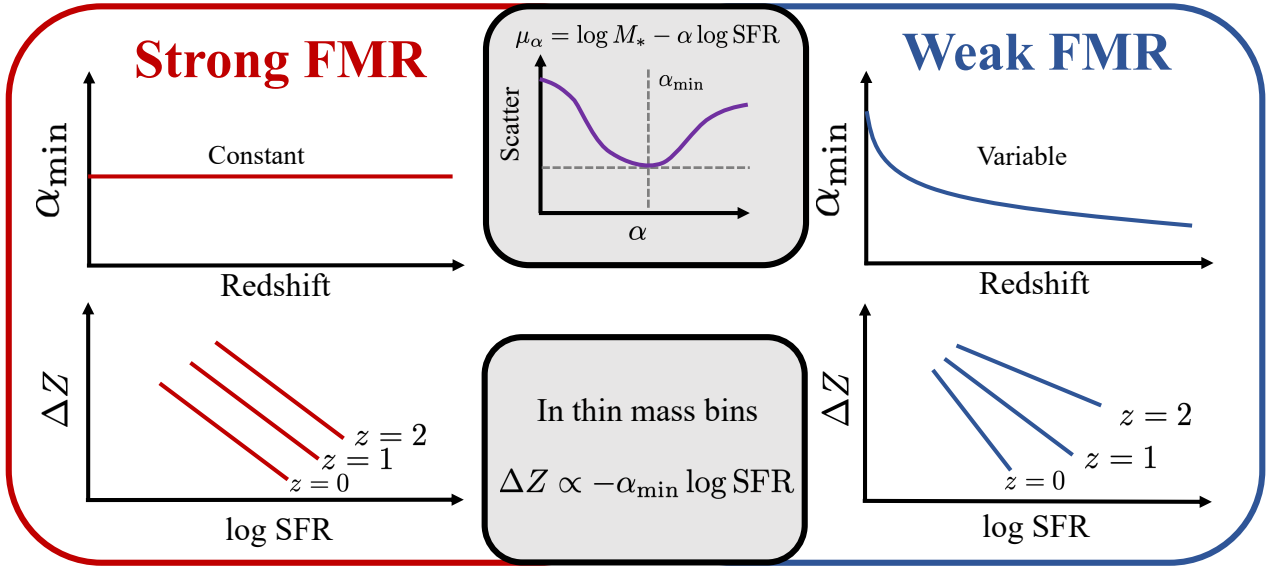
Figure 5. Summary of Key Points. The strong FMR (left, red) is where $\alpha_{\min}$, a parameter tuned to minimise scatter about the MZR, is constant as a function of redshift. Consequently, in thin mass bins, the offsets from the MZR, ΔZ, as a function of (log) SFR have roughly the same slope at all redshifts (although there is a dependence on the slope of the FMR, see Section 4.1 for more details). The weak FMR (right, blue) is where $\alpha_{\min}$ varies as a function of redshift. In this scenario, the individual redshift's have different strengths of correlations between offsets from the MZR and (log) SFR.

the sensitivity of $\alpha_{\min}$ to the input physics within the simulation models becomes clear. The redshift-dependent winds in TNG work to increase wind velocities at low redshift which suppresses star formation. This star formation suppression likely plays a significant role in the overall decrease of $\alpha_{\min}$ seen at low redshifts in TNG.

All three models examined here rely on effective equation of state sub-grid models for the dense, unresolved ISM (Springel & Hernquist 2003 for Illustris/TNG and Schaye & Dalla Vecchia 2008 for EAGLE). In recent years, however, high-resolution simulation modelling has begun to directly resolve the sites of star formation (e.g., Feedback In Realisitc Environments model; Hopkins et al. 2014). The stellar feedback in such simulations is much burstier than in the models presented here. We believe that bursty stellar feedback events should suppress $\alpha_{\min}$ values compared to Illustris, TNG, and EAGLE. Subgrid pressurization lends support to the ISM that is not coupled to star formation, and therefore blunts rapid variations in star formation and stellar feedback. Models without subgrid pressurization (like FIRE) do not have this source of ISM support, and therefore exhibit more rapid (i.e., bursty) variations in star formation and stellar feedback. Bursts may therefore curtail the effectiveness of star formation rates in regulating the gas-phase metallicity of a galaxy. Therefore the redshift variations in $\alpha_{\min}$ may be able to provide constraining power on the extent to which galaxies' feedback is more bursty or smooth. Although it should be noted that even within these smooth feedback models there is some disparity.

5 CONCLUSIONS

We select central star forming galaxies with stellar mass $8.0 < \log(M_* \, [M_\odot]) < 12.0$ with gas mass $\log(M_{\rm gas} \, [M_\odot]) > 8.5$ from $z = 0 - 8$ in the cosmological simulations Illustris, IllustrisTNG, and EAGLE. We investigate the extent to which the M10 parameterisation (see Equation 1; μ_αZR) of the fundamental metallicity relation (FMR; Equation 1) holds. The parameter of merit in the μ_αZR is $\alpha_{\min}$, which is a parameter tuned to minimize scatter in the relation.

Physically, $\alpha_{\min}$ sets a projection direction of the mass-metallicity-SFR space to a 2D space with minimal scatter. Many observational studies have claimed that this projection direction does not evolve with redshift (Mannucci et al. 2010; Cresci et al. 2019).

We discuss a new framework in which to examine the μ_αZR as a superset of the MZR ($\alpha = 0$) and FMR ($\alpha \neq 0.0$). We further define both a strong and weak FMR. A strong FMR indicates that $\alpha_{\min}$ is constant as a function of redshift. Conversely, the weak FMR is where $\alpha_{\min}$ varies with redshift (see Figure 1 for complete illustrated relationship of μ_αZR). More generally, the strong FMR states the the M10 parameterisation can describe both the scatter and noramlsation of the MZR at the same time.

Our conclusions are as follows:

- We find that $\alpha_{\min} \neq 0$ for all redshifts in Illustris, TNG, and EAGLE. This shows that there is an FMR in each of these simulations. We note, however, that the uncertainty in $\alpha_{\min}$ in TNG at $z = 0$ includes $\alpha_{\min} = 0.0$. We attribute this to the increased suppression of low redshift star formation in the TNG model.

- Furthermore, we find that there is non-negligible evolution in $\alpha_{\min}$ as a function of redshift (Figure 2). This result suggests that the FMR in Illustris, TNG, and EAGLE is a weak FMR.

- We find that the weak FMR ($\alpha_{\min}$ determined at each redshift independently) consistently reduces scatter around $10 - 30\%$ compared to the the MZR (left panel of Figure 3). The strong FMR also reduces the scatter compared to the MZR, albeit to a lesser extent than the weak FMR. At high-z in EAGLE, however, using the strong FMR actually *increases* scatter compared to the MZR (centre panel of Figure 3). Overall, we find that at $z \gtrsim 3$ fitting galaxies with a weak FMR can reduce scatter $\sim 5 - 40\%$ more than using the strong FMR (right panel of Figure 3).

- We suggest that the interpretation of $\alpha_{\min}$ variations is more well-understood in the context of the slope of ΔZ (offsets from the MZR) as a function of log SFR (see Figure 4). In this context, the weak FMR suggest that the relationship between metallicity and SFR changes through cosmic time, whereas the strong FMR suggests that

it does not change. We also show that the slope in $\Delta Z - \log$ SFR space is proportional to α_{min} (see Equation 3).

Obtaining one relationship that describes the metal evolution of all galaxies across time is an ambitious goal. It is worth appreciating how reasonably well a simple linear combination of two parameters can begin to achieve that goal at low redshift. Yet it is not perfect. To begin to rectify this, we develop a substantial overhaul to the current FMR paradigm (summarized in Figure 5). The results from this work show that Illustris, TNG, and EAGLE indicate deviations from the strong FMR. It is presently unclear whether the same is true in observations. Understanding whether the FMR in observations is weak or strong will aid in being able to understand the recent *JWST* observations suggesting high redshift FMR evolution.

DATA AVAILABILITY

The reduced data products, analysis scripts, and figures are all available publicly at https://github.com/AlexGarcia623/Does-the-FMR-evolve-Simulations/. Data from Illustris and IllustrisTNG is publicly available on each project's respective website. Illustris: https://www.illustris-project.org/data/ and IllustrisTNG: https://www.tng-project.org/data/. Similarly, data products from the EAGLE simulations are available for public download via the Virgo consortium's website: https://icc.dur.ac.uk/Eagle/database.php

REFERENCES

Andrews B. H., Martini P., 2013, ApJ, 765, 140
Belli S., Jones T., Ellis R. S., Richard J., 2013, ApJ, 772, 141
Blanc G. A., Lu Y., Benson A., Katsianis A., Barraza M., 2019, ApJ, 877, 6
Bothwell M. S., Maiolino R., Kennicutt R., Cresci G., Mannucci F., Marconi A., Cicone C., 2013, MNRAS, 433, 1425
Bothwell M. S., Maiolino R., Peng Y., Cicone C., Griffith H., Wagg J., 2016, MNRAS, 455, 1156
Chabrier G., 2003, PASP, 115, 763
Crain R. A., et al., 2015, MNRAS, 450, 1937
Cresci G., Mannucci F., Curti M., 2019, A&A, 627, A42
Curti M., Mannucci F., Cresci G., Maiolino R., 2020, MNRAS, 491, 944
Curti M., et al., 2023, arXiv e-prints, p. arXiv:2304.08516
Dalcanton J. J., 2007, ApJ, 658, 941
Davé R., Finlator K., Oppenheimer B. D., 2011, MNRAS, 416, 1354
Davé R., Rafieferantsoa M. H., Thompson R. J., Hopkins P. F., 2017, MNRAS, 467, 115
Davis M., Efstathiou G., Frenk C. S., White S. D. M., 1985, ApJ, 292, 371
Dayal P., Ferrara A., Dunlop J. S., 2013, MNRAS, 430, 2891
De Rossi M. E., Theuns T., Font A. S., McCarthy I. G., 2015, MNRAS, 452, 486
De Rossi M. E., Bower R. G., Font A. S., Schaye J., Theuns T., 2017, MNRAS, 472, 3354
De Rossi M. E., Bower R. G., Font A. S., Schaye T., 2018, Boletin de la Asociacion Argentina de Astronomia La Plata Argentina, 60, 121
Dolag K., Borgani S., Murante G., Springel V., 2009, MNRAS, 399, 497
Donnari M., et al., 2019, MNRAS, 485, 4817
Ellison S. L., Patton D. R., Simard L., McConnachie A. W., 2008, ApJ, 672, L107
Elmegreen B. G., 1999, ApJ, 527, 266
Fontanot F., et al., 2021, MNRAS, 504, 4481
Garcia A. M., et al., 2023, MNRAS, 519, 4716
Garcia A. M., et al., 2024, arXiv e-prints, p. arXiv:2401.12310
Genel S., et al., 2014, MNRAS, 445, 175
Heintz K. E., et al., 2023, Nature Astronomy, 7, 1517
Hemler Z. S., et al., 2021, MNRAS, 506, 3024
Hopkins P. F., Kereš D., Oñorbe J., Faucher-Giguère C.-A., Quataert E., Murray N., Bullock J. S., 2014, MNRAS, 445, 581
Kewley L. J., Nicholls D. C., Sutherland R. S., 2019, ARA&A, 57, 511
Koeppen J., 1994, A&A, 281, 26
Lacey C. G., Fall S. M., 1985, ApJ, 290, 154
Langeroodi D., Hjorth J., 2023, arXiv e-prints, p. arXiv:2307.06336
Langeroodi D., et al., 2023, ApJ, 957, 39
Lara-López M. A., et al., 2010, A&A, 521, L53
Lee H., Skillman E. D., Cannon J. M., Jackson D. C., Gehrz R. D., Polomski E. F., Woodward C. E., 2006, ApJ, 647, 970
Lilly S. J., Carollo C. M., Pipino A., Renzini A., Peng Y., 2013, ApJ, 772, 119
Looser T. J., D'Eugenio F., Piotrowska J. M., Belfiore F., Maiolino R., Cappellari M., Baker W. M., Tacchella S., 2024, arXiv e-prints, p. arXiv:2401.08769
Maiolino R., Mannucci F., 2019, A&ARv, 27, 3
Maiolino R., et al., 2008, A&A, 488, 463
Mannucci F., Cresci G., Maiolino R., Marconi A., Gnerucci A., 2010, MNRAS, 408, 2115
Marinacci F., et al., 2018, MNRAS, 480, 5113
McAlpine S., et al., 2016, Astronomy and Computing, 15, 72
Naiman J. P., et al., 2018, MNRAS, 477, 1206
Nakajima K., Ouchi M., Isobe Y., Harikane Y., Zhang Y., Ono Y., Umeda H., Oguri M., 2023, ApJS, 269, 33
Nelson D., et al., 2018, MNRAS, 475, 624
Nelson D., et al., 2019a, Computational Astrophysics and Cosmology, 6, 2
Nelson D., et al., 2019b, MNRAS, 490, 3234
Nelson E. J., et al., 2021, MNRAS, 508, 219
Pillepich A., et al., 2018a, MNRAS, 473, 4077
Pillepich A., et al., 2018b, MNRAS, 475, 648
Pillepich A., et al., 2019, MNRAS, 490, 3196
Pistis F., et al., 2023, arXiv e-prints, p. arXiv:2312.00930
Salim S., Lee J. C., Davé R., Dickinson M., 2015, ApJ, 808, 25
Sanders R. L., et al., 2015, ApJ, 799, 138
Sanders R. L., et al., 2018, ApJ, 858, 99
Sanders R. L., et al., 2021, ApJ, 914, 19
Sanders R. L., Shapley A. E., Topping M. W., Reddy N. A., Brammer G. B., 2023, arXiv e-prints, p. arXiv:2303.08149
Savaglio S., et al., 2005, ApJ, 635, 260
Schaye J., 2004, ApJ, 609, 667
Schaye J., Dalla Vecchia C., 2008, MNRAS, 383, 1210
Schaye J., et al., 2015, MNRAS, 446, 521
Scholte D., Saintonge A., 2023, MNRAS, 518, 353
Shapley A. E., Reddy N. A., Sanders R. L., Topping M. W., Brammer G. B., 2023, arXiv e-prints, p. arXiv:2303.00410
Somerville R. S., Davé R., 2015, ARA&A, 53, 51
Springel V., 2005, MNRAS, 364, 1105
Springel V., 2010, MNRAS, 401, 791
Springel V., Hernquist L., 2003, MNRAS, 339, 289

Springel V., White M., Hernquist L., 2001, ApJ, 549, 681
Springel V., et al., 2018, MNRAS, 475, 676
Torrey P., Vogelsberger M., Genel S., Sijacki D., Springel V., Hernquist L.,
  2014, MNRAS, 438, 1985
Torrey P., et al., 2018, MNRAS, 477, L16
Tremonti C. A., et al., 2004, ApJ, 613, 898
Vogelsberger M., Genel S., Sijacki D., Torrey P., Springel V., Hernquist L.,
  2013, MNRAS, 436, 3031
Vogelsberger M., et al., 2014a, MNRAS, 444, 1518
Vogelsberger M., et al., 2014b, Nature, 509, 177
Weinberger R., et al., 2017, MNRAS, 465, 3291
Wiersma R. P. C., Schaye J., Theuns T., Dalla Vecchia C., Tornatore L., 2009,
  MNRAS, 399, 574
Wuyts E., Rigby J. R., Sharon K., Gladders M. D., 2012, ApJ, 755, 73
Yang N., Scholte D., Saintonge A., 2024, MNRAS, 527, 11043
Zahid H. J., Kewley L. J., Bresolin F., 2011, ApJ, 730, 137
Zahid H. J., Dima G. I., Kudritzki R.-P., Kewley L. J., Geller M. J., Hwang
  H. S., Silverman J. D., Kashino D., 2014, ApJ, 791, 130

APPENDIX A: (LACK OF) DEPENDENCE ON SPECIFIC STAR FORMATION MAIN SEQUENCE

Part of our galaxy selection criteria includes selecting star forming galaxies (see Section 2.4 for full details). Our method of selecting these galaxies uses a specific star formation main sequence cut. The sSFMS selection includes a cut excluding galaxies 0.5 dex below the median relation. In this appendix, we consider three additional variations on this cut (following from Garcia et al. 2024): (i) a more restrictive cut of all galaxies 0.1 dex below the median relation, (ii) a less restrictive cut of all galaxies 1.0 dex below the median relation, and (iii) a very liberal cut of all galaxies with non-zero SFRs. We show the resultant α_{min} values from these cuts in Figure A1. The uncertainty bars on α_{min} overlap for all redshift bins in all three analysed simulations with all four cuts. However, there are three cases in which the derived α_{min} value itself varies significantly for the SFR > 0 cut: TNG $z = 1$ and 2 as well as EAGLE $z = 0$. In these three cases, α_{min} is significantly offset from the errorbars of at least two of the three other cuts. The uncertainties using the SFR > 0 cut in these three cases are quite large. This suggests that the overall change in scatter when using the SFR > 0 cut versus another cut is marginal. We therefore conclude that, while the derived α_{min} value may change, these changes have no qualitative bearing on the results presented in this work.

APPENDIX B: HIGHER ORDER POLYNOMIAL FIT

M10 determined residuals in the scatter about a fourth-order polynomial instead of a linear regression. This practice is not consistent through all works using the μ_α 2D projection of the FMR, however. For example, recent *JWST* observational papers (e.g., Nakajima et al. 2023; Langeroodi & Hjorth 2023) adopt a linear regression definition of the FMR from Andrews & Martini (2013). We show that using a linear regression does not significantly change the projection of least scatter in Illustris, TNG, and EAGLE in Figure B1.

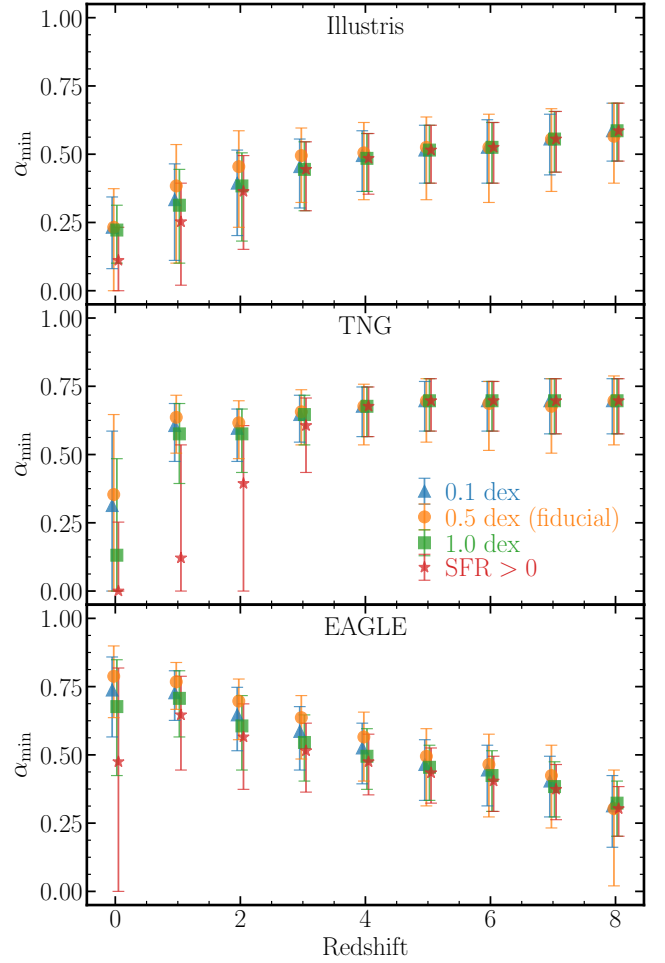This paper has been typeset from a TₑX/LATₑX file prepared by the author.

Figure A1. Determination of α_{min} as a function of redshift for Illustris (top), TNG (centre), and EAGLE (bottom) for the four different sSFMS variations.
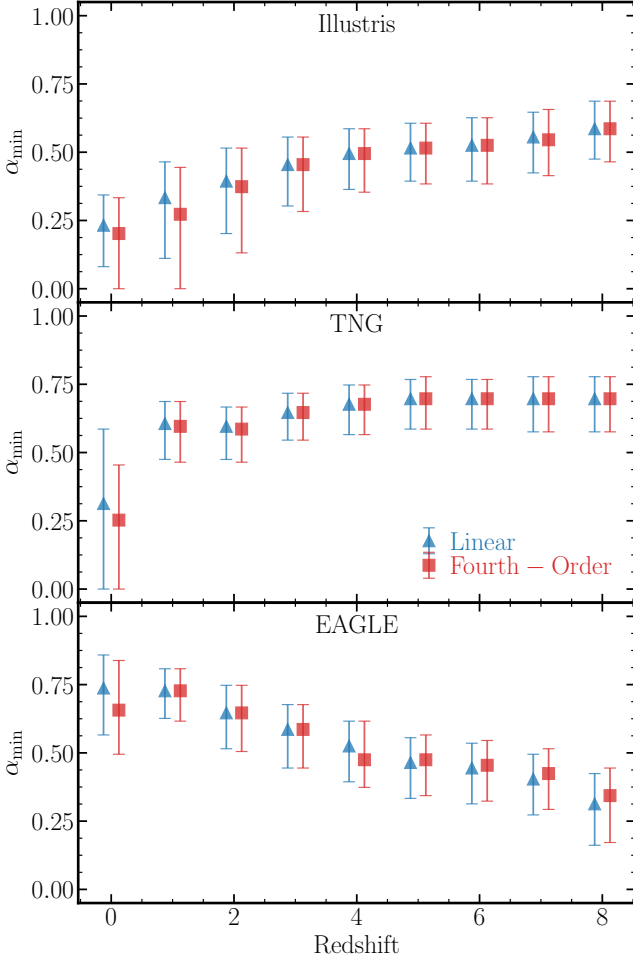
Figure B1. Determination of α_{min} as a function of redshift for Illustris (top), TNG (centre), and EAGLE (bottom) using a linear regression (blue triangles) and fourth-order polynomial regression (red squares).